



Highly nanotextured nickel-electroplated bismuth vanadate micropillars for hotspot removal via air- and spray-cooling

Taegun Kim^{a,1}, Chanwoo Park^{a,1}, Minwoo Kim^a, Seongpil An^{b,*}, Sam S. Yoon^{a,*}

^aSchool of Mechanical Engineering, Korea University, Seoul 02841, Republic of Korea

^bSKKU Advanced Institute of Nanotechnology (SAINT) and Department of Nano Engineering, Sungkyunkwan University (SKKU), Suwon 16419, Republic of Korea

ARTICLE INFO

Article history:

Received 4 December 2019

Revised 24 March 2020

Accepted 30 March 2020

Keywords:

Heat dissipation

Bismuth vanadate (BiVO₄)

Micropillars

Heat spreader

Cooling film

Electrospraying

Electroplating

ABSTRACT

Overheating and hotspots in high-power and high-density microelectronics can cause device malfunction and shortened device lifespans; however, cooling films with highly textured surfaces may alleviate these concerns by efficiently removing and dissipating heat. In this study, the electrospraying of bismuth vanadate (BiVO₄) facilitated the formation of micropillars via diffusion-limited aggregation, yielding a highly textured surface. This was subsequently metallized via Ni electroplating for use as an efficient heat-removing and -spreading film. Because of their large surface areas, the BiVO₄ micropillars acted not only as heat removers and spreaders, but also as an electrically insulating layer that could prevent unexpected electrical shocks to the device underneath the cooling film. The thermal resistance, electrical insulating properties, heat dissipating features, and convective heat transfer coefficient of the BiVO₄-Ni bilayer films were studied, and the films were characterized using X-ray photoelectron spectroscopy, X-ray diffraction, scanning electron microscopy, and transmission electron microscopy. The obtained cooling films were very flexible and light and could be readily attached to portable electronics without adding much weight. Such films could become commercially viable solutions for the problem of overheating in portable electronics.

© 2020 Elsevier Ltd. All rights reserved.

1. Introduction

The miniaturization of electronic devices inevitably entails significant thermal management challenges because the power density and heat flux of microprocessors are increased substantially with decreasing device size [1]. According to Moore's law, the heat load on microprocessors increases as the demand for large transistor numbers, high processor speeds, and small device sizes increases [2,3]. While module power densities range from 10 to 10² W cm⁻² [4], areas of high local power density, known as "hotspots" or "fireballs," can have densities up to ~10³ W cm⁻² [5]. However, the high peak temperatures of such hotspots raise reliability and performance concerns [4,6–13]. Furthermore, these hotspots could cause processor malfunction and eventual shut-down of the entire device [4].

While liquid cooling can be utilized to mitigate the temperature of hotspots, this is impractical for portable devices because of the associated weight, cost, and reliability concerns of liquid cooling

systems. In addition, hotspots occur locally, whereas liquid cooling is suitable for cooling large modules, and not small portable electronics. Air cooling with fans and heatsinks can also be employed; however, the addition of such devices introduces noises and increases the overall production cost of portable electronics, which renders them impractical and expensive [14].

Heat pipes exploiting latent heats of evaporation are often used for portable electronics, but they are more suitable for module cooling than for local cooling [4]. Thermoelectric refrigerators, also known as Peltier coolers, utilize an expanded electron gas in the solid state that flows across a semiconducting material (i.e., Bi₂Te₃/Sb₂Te₃, PbSeTe/PbTe, or SiGe/Si) [2,15–18]. Thermoelectric cooling is locally selective, independent of gravity, fast, and highly reliable because of the intrinsic solid state of the cooling agent [19]. However, thermoelectric coolers require additional power sources, which add to the total heat requiring removal; therefore, these coolers are impractical for many applications. Moreover, the costs associated with thermoelectric cooling devices are high because they require the additional installation of heat sinks. Therefore, the development of light, small, easily attachable thermoelectric thin films that do not use heat sinks or/and fans and can be locally and readily installed is imperative.

* Corresponding authors.

E-mail addresses: esan@skku.edu (S. An), skyoona@korea.ac.kr (S.S. Yoon).

¹ These authors have contributed equally.

Heat sinks are installed to increase the total surface area and maximize the total heat-exchange surface area. The total surface area per volume of a material can be increased by introducing microscale-textured surfaces. For a device with high surface area per unit volume, the local hotspot temperature is relatively low. In this study, we propose a method to maximize the surface area of the cooling film by the introduction of arrays of micropillars. This increase in the surface area increased the effective heat transfer coefficient, which, in turn, decreased the hotspot temperature. In addition, the micropillars were electroplated with Ni to increase the thermal conductivity of the cooling film and to ensure efficient heat spreading. Consequently, both heat removal via convective cooling and heat spreading via enhanced conduction could be achieved.

Micropillars were fabricated via the electro spraying of bismuth vanadate (BiVO_4), which utilized the diffusion-limited aggregation phenomenon [20–22]. The BiVO_4 micropillars were subsequently electroplated with Ni. The thermal conductivity of Ni is sufficiently high to ensure heat transfer in the in-plane direction. The introduction of the Ni-electroplated BiVO_4 , or Ni- BiVO_4 bilayer, achieved two objectives: The BiVO_4 micropillars removed heat via convection, and the Ni coating spread heat via conduction. Spreading of heat is particularly important when electronic devices are completely sealed to make them impervious to water, therefore permitting no inflow and outflow. In such scenarios, hotspots can only be cooled by spreading their heat to a solid medium via conduction. Thus, the mechanisms for removing and spreading of heat operate independently.

Carbon materials are often used as heat spreading materials [23–29]. However, it is difficult to deposit carbon materials without the use of additives, which generally increase the thermal resistance of films. Electroplating facilitates in situ adhesion between Ni and BiVO_4 without additives; therefore, the obtained BiVO_4 -Ni bilayers are additive-free.

The use of highly textured BiVO_4 micropillars as efficient heat removers combined with Ni as a heat spreader has never been documented. The fabricated bilayer films are thin, light, flexible, attachable, electrically insulating, heatsink-free, and fan-free, and thus could be commercially viable. Because of the unique nanotextured surfaces of the BiVO_4 -Ni cooling films, they could also be used for spray cooling, in which the wettability of droplets becomes important in the heat-transfer phenomena [30,31]. The textured surface of the BiVO_4 -Ni films promotes wetting and subsequent heat transfer by the rapidly boiling of liquid droplets that come into contact with it. Therefore, the fabricated cooling films could be used not only for air-cooling, but also for spray cooling, as demonstrated herein.

2. Experimental methods

2.1. Electro sprayed BiVO_4 micropillar film

Electrostatic spraying was the first step employed for fabricating the heat spreading films. The precursor solution for fabricating the BiVO_4 micropillar films was obtained by mixing 1.08 g bismuth (III) nitrate pentahydrate ($\geq 98\%$, Sigma-Aldrich, USA), 0.78 g vanadium (III) acetylacetonate (Sigma-Aldrich, USA), and 10 mL acetic acid (99.7%, Samchun Chemicals, Republic of Korea), and subsequently stirring the mixed solution for 60 min at 25 °C. The BiVO_4 films were fabricated by electrostatically spraying the precursor solution onto Cu foils ($3 \times 3 \text{ cm}^2$). Table 1 lists the experimental parameters for the electrostatic spraying process used to fabricate the BiVO_4 micropillar films. The steps of the electrostatic spraying process have been described in detail in some of our previously published papers [20–22]. The precursor solution was deposited on the Cu foils for 60 min at the flow rate of $80 \mu\text{L h}^{-1}$. A high

Table 1
Conditions for fabricating BiVO_4 films via electrostatic spray deposition.

Parameter	Value
Substrate	Cu foil
Applied voltage [kV]	11
Cu substrate dimensions [cm^2]	3×3
Nozzle to substrate distance [cm]	5
Coating time [min]	60
Temperature of substrate [°C]	80
Annealing temperature [°C]	350

voltage of 11 kV was applied to the nozzle to form and ensure stable Taylor cones. The temperature of the Cu foil substrate was maintained at 80 °C during spraying. Fig. 1a depicts the schematic of the electro spray deposition process for fabricating the BiVO_4 micropillars.

2.2. Ni electroplating on BiVO_4 films

A Ni electroplating solution was prepared and used to deposit Ni layers on the BiVO_4 micropillar films. Ni was chosen because its corrosion resistance prolongs the film lifespan. The Ni precursor solution was prepared by adding 8 g nickel chloride hexahydrate ($\text{NiCl}_2 \cdot 6\text{H}_2\text{O}$, 99.9%, Sigma Aldrich, USA) and 8 g boric acid (H_3BO_3 , 99.97%, Sigma Aldrich, USA) to deionized (DI) water. The final volume of the solution was set to 160 mL by adjusting the amount of DI water, and the solution was stirred at 500 rpm and 60 °C for 30 min. Afterward, 22 mL aqueous HCl (2 mL HCl+20 mL DI water) and 22 mL aqueous NH_4OH (2 mL NH_4OH +20 mL DI water) were added to the pre-mixed $\text{NiCl}_2 \cdot 6\text{H}_2\text{O}/\text{H}_3\text{BO}_3$ solution. As in Fig. 1b, the fabricated BiVO_4 micropillar film was immersed in the electroplating solution and faced with a Ni foil ($3 \times 3 \text{ cm}^2$) to initiate the electroplating process. Subsequently, Ni was electroplated on the BiVO_4 micropillars only. It should be noted that the Cu foil was not electroplated with Ni. The Cu foil was electro sprayed to produce BiVO_4 micropillars, which were later electroplated with nickel to eventually fabricate the Cu/ BiVO_4 /Ni multiplayer film. An electric current (0.018 A; current density $I_{ep} = 2 \text{ mA cm}^{-2}$ based on the total dimensions of the bare BiVO_4 film) was applied for 0, 5, 15, and 60 min using a direct-current (DC) power supply (E3644A, Agilent Technologies, USA) (Fig. 1b). The specimens obtained after $t_{ep} = 0, 5, \text{ and } 15$ min of Ni electroplating are hereafter referred to as Ni-0, Ni-5, and Ni-15, respectively. The image on the left side of Fig. 1c depicts the bending test of the BiVO_4 -Ni film where the radius of curvature (R_a) is approximately 5 mm. The center image depicts the bare BiVO_4 film, while the inset displays a light-emitting diode (LED) turning on upon application of a voltage to the BiVO_4 -Ni film, confirming the electrical conductivity of the Ni- BiVO_4 film. The scanning electron microscopy (SEM) image (right panel in Fig. 1c) illustrates the top surface morphology of the BiVO_4 -Ni film.

2.3. Heat transfer experiment

Fig. 2 depicts the experimental setup used for the heat-transfer experiment. A one-dimensional linear Ni-Cr wire ($\rho = 5.73 \Omega \text{ m}^{-1}$ and diameter = 1 mm) was placed on an Al_2O_3 substrate. A DC power supply source (E3644A, Agilent Tech, US) was used to apply voltage to the heating wire. The supplied current (I) and voltage (V) were measured by a Clamp-On AC/DC HiTester (HIOKI 3288, HIOKI, JAPAN) and a Digital multimeter (HIOKI DT4212, HIOKI, JAPAN), respectively. The total electrical heating power was $q_{exp} = IV$. The temperatures of all samples were measured using a K-type thermocouple (probe size of 1 mm \times 150 mm) and recorded using a data logger (GL-240, Graphtec, USA). The inset

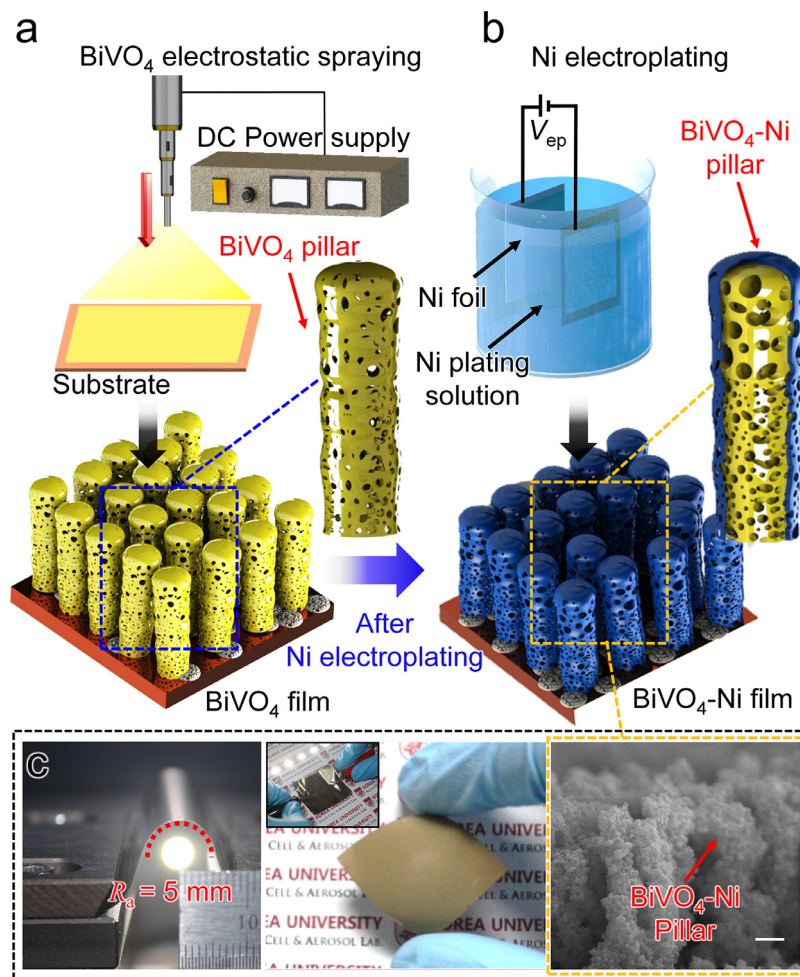


Fig. 1. Detailed schematics of manufacturing the cooling film test modules: (a) electrostatic spraying of BiVO_4 on Cu foil and (b) electroplating of Ni on BiVO_4 pillars (V_{ep} is the electroplating potential). (c) Left: Bending test of the BiVO_4 -Ni film (R_a is the radius of curvature), Center: Photographs of BiVO_4 and BiVO_4 -Ni films (inset), Right: SEM image of BiVO_4 with Ni-5 film. Note that the BiVO_4 pillars are not hollow and that Ni is electroplated on the BiVO_4 surface, not inside the pillars.

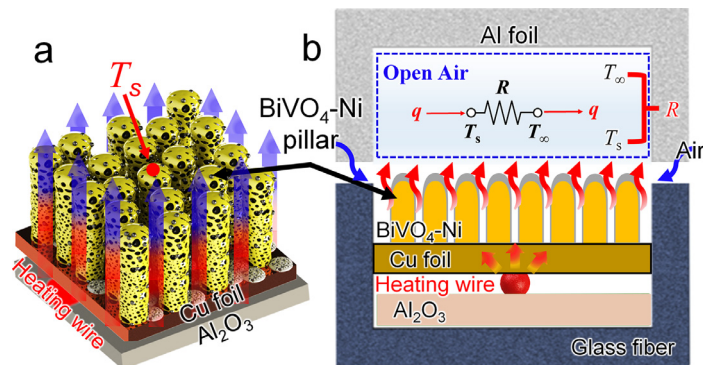


Fig. 2. Detailed schematics of (a) the multilayered heat spreading BiVO_4 -Ni film and (b) heat-transfer experiment using the heat spreading film. Here q , R , T_s , and T_∞ denote the power, resistance of the heating wire, surface temperature, and ambient temperature (25 °C), respectively. Note that T_s refers to the surface temperature of the tops of the BiVO_4 pillars.

of the image on the right side in Fig. 2 illustrates the electrical circuit associated with the vertical convective cooling process from the surface temperature T_s to the ambient temperature T_∞ . The straight heating wire was placed between the Al_2O_3 substrate and Cu foil, wherein the heat was transferred three-dimensionally. However, for convenience of calculation, we have applied a one-dimensional quasi-analysis from T_s to T_∞ to measure the values of the heat-transfer coefficients [32]. Experiments were conducted to confirm that the changes in temperature from T_s to T_∞ were

caused by convection, which was attributed to the use of the BiVO_4 -Ni film. To prevent radiative heat loss, the chamber was covered with Al foil, but ventilation was allowed for convective cooling. Moreover, the use of glass fiber insulation encasing the Al_2O_3 substrate at the bottom minimized the overall heat loss from the experimental setup. This experiment was performed to analyze the dependence of the natural vertical convective cooling effect of the ambient atmosphere on the BiVO_4 /Ni-textured surface.

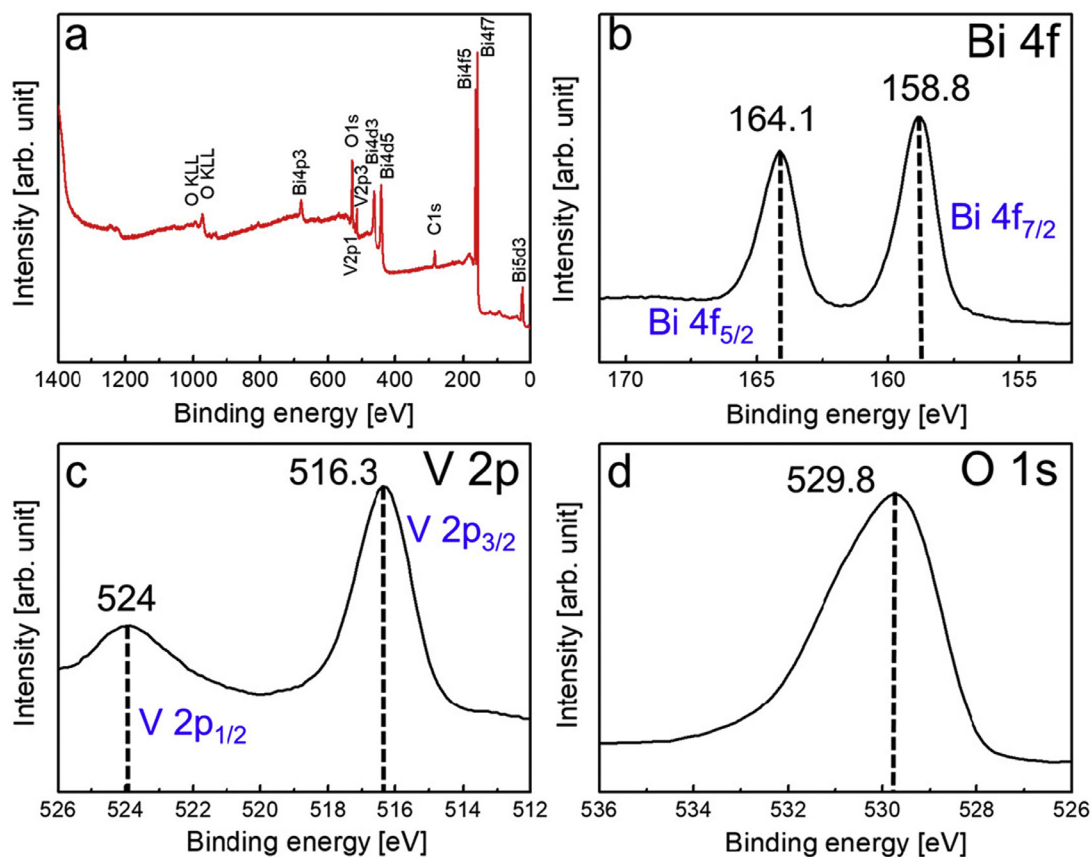


Fig. 3. XPS profiles of bare BiVO_4 film: (a) survey, (b) Bi 4f, (c) V 2p, and (d) O 1s.

2.4. Characterization of BiVO_4 -Ni films

A high-resolution scanning electron microscopy (HR-SEM; XL30 SFEG, Phillips Co., Netherlands) instrument operated at 15 kV was used to analyze the morphology of the surfaces of the multilayered heat spreading BiVO_4 -Ni films. The crystallinity of the BiVO_4 -Ni films was investigated using X-ray diffraction (XRD; SmartLab, Rigaku, Japan). A transmission electron microscopy (TEM; JEM 2100F, JEOL, Inc., Japan) apparatus equipped with an energy-dispersive X-ray spectroscopy (EDS) unit was used to analyze the surface morphologies and elemental distributions of the BiVO_4 -Ni films.

An infrared (IR) camera (FLIR-E63900, FLIR System, Inc., USA) was used to visualize the changes in heat transfer over time. The heat sensitivity of the IR camera was approximately 30 mK at 25 °C, and its error range was approximately 1%. To perform the initial calibration of the IR camera, the object temperature was confirmed using a thermocouple. The temperature values measured using the thermocouple and those estimated using the IR images were synchronized by adjusting the emissivity (ϵ) of the camera. To avoid the thermal remainder and interference of other ambient light sources, ϵ was set to 1. A high-speed camera (Phantom 6117M, Phantom, USA) was used to visualize the drop impact and spray cooling test results.

3. Results and discussion

We used X-ray photoelectron spectroscopy (XPS) to investigate the oxidation states of the elements comprising the BiVO_4 film. Fig. 3a illustrates the survey spectrum of the bare BiVO_4 film (Ni-0 specimen, cf. Section 2.2), in which the Bi 4f, V 2p, and O 1s peaks can be observed. The Bi 4f, V 2p, and O 1s binding energy peaks

are analyzed using the individual spectrum of each respective element. Fig. 3b presents the XPS core-level profile of Bi, where the presence of two peaks at 164.1 and 158.8 eV, corresponding to Bi 4f_{5/2} and Bi 4f_{7/2}, respectively, confirm the presence of Bi³⁺ ions in the BiVO_4 film. Fig. 3c depicts the V 2p XPS peaks at 524 and 516.3 eV, ascribed to the V 2p_{1/2} and V 2p_{3/2} orbitals. The difference in the binding energies of the two V 2p peaks (~7.7 eV) suggests the oxidation state of V⁵⁺. Lastly, the O 1s peak at 529.8 eV in Fig. 3d is well-matched with those observed from metal oxides, and is assigned to the lattice O.

Fig. 4a depicts the XRD patterns of Ni-0 and Ni-5. The XRD patterns, measured in the 2θ range of 10–80° at the scanning resolution of 0.01°, of both films match that of the monoclinic crystal structure of BiVO_4 . The diffraction peaks at 28.9°, 30.6°, 34.6°, 35.2°, 39.9°, 42.6°, 46.8°, 50.7°, 53.4°, 58.3°, and 59.5°, corresponding to the (121), (040), (200), (002), (211), (231), (240), (202), (161), (321), and (123) planes, respectively, of BiVO_4 (JCPDS 14-0688), appear in the XRD patterns of both Ni-0 [21] and Ni-5 (Fig. 4a). Thus, the Ni deposited over the BiVO_4 film does not affect the crystallinity of BiVO_4 . However, the intensity of the above-mentioned peaks is higher in the Ni-5 pattern than in that of Ni-0. The increased intensity may arise from the higher atomic scattering caused by Ni [33]. Particularly, the intensities of the 43.7°, 51°, and 77° peaks, corresponding to the (111), (200), and (220) planes of Ni (JCPDS 04-0836), respectively, are significantly higher in the XRD profile of Ni-5 than in that of Ni-0.

The Raman spectra of the Ni-0 and Ni-5 films are depicted in Fig. 4b. The peaks at 209, 327, 367, and 823 cm^{-1} are typical vibrational modes of the BiVO_4 structure. The peak at 209 cm^{-1} belongs to the external vibrational mode (rotation/translation) of BiVO_4 . The two peaks at 327 and 368 cm^{-1} are assigned to the asymmetric (B_g) and symmetric (A_g) modes of the VO_4^{3-} ion, re-

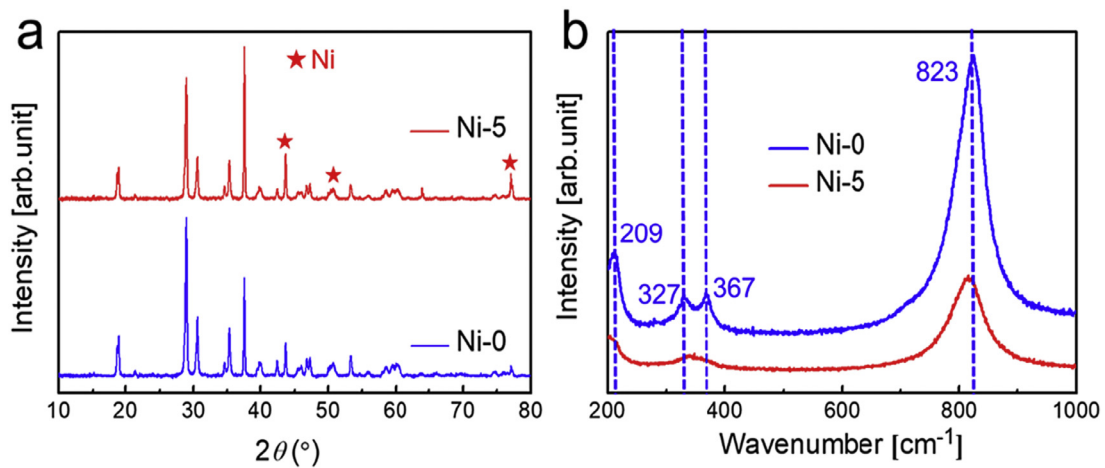


Fig. 4. (a) XRD patterns and (b) Raman spectra of bare BiVO_4 film (Ni-0) and BiVO_4 -Ni film electroplated for 5 min (Ni-5).

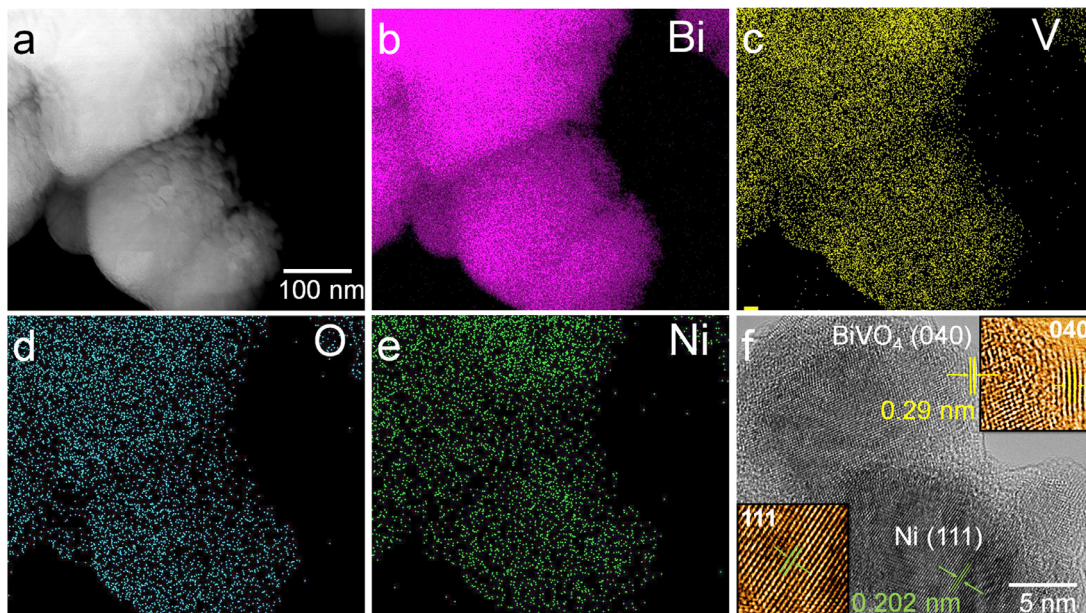


Fig. 5. (a) Cross-sectional TEM image of BiVO_4 electroplated with Ni for 5 min (Ni-5). The corresponding elemental mappings of (b) Bi, (c) V, (d) O, and (e) Ni. (f) High-resolution TEM image of the Ni-5 case, where the lattice d -spacings of the (040) plane of BiVO_4 and (111) plane of Ni are marked. Note that all elements (Bi, V, O, Ni) are uniformly distributed on the pillar.

spectively. The sharp dominant peak at 823 cm^{-1} in the spectrum of Ni-0 is attributed to the symmetric V–O stretching mode [21]. The intensities of the peaks in the Raman spectrum of Ni-5 are lower than those in the spectrum of Ni-0; this may arise from the imperfect resonance effect, attributed to the presence of Ni in the Ni-5 sample. The peak at approximately 823 cm^{-1} in the spectrum of Ni-5, which is associated with the V–O bonds, is shifted to the left compared with the peak in the spectrum of Ni-0; this is attributed to the V–O bond length in the Ni-5 specimen being shorter than that in Ni-0.

Fig. 5 illustrates the high-magnification TEM image, elemental mappings, and high-resolution TEM (HR-TEM) image of the Ni-5 film. For imaging, the BiVO_4 -Ni pillars were cut from the Ni-5 film via focused ion beam milling. Fig. 5b–e present the Bi, V, O, and Ni elemental mappings of Ni-electroplated BiVO_4 nanoparticles deposited on a Cu foil. The HR-TEM image of the Ni-5 film is presented in Fig. 5f. The fringes of the d -spacings of 0.29 and 0.202 nm correspond to the (040) plane of BiVO_4 and (111) plane of Ni, respectively. These results are consistent with the XRD data

in Fig. 4a and verify the formation of the BiVO_4 -Ni pillars via electrostatic spraying followed by Ni electroplating.

Fig. 6a–d illustrate the time-dependent surface temperatures (T_s) with different heating powers ($0.160 \leq q_{\text{exp}} \leq 0.222 \text{ W}$). Here, $\Delta T = T_s - T_\infty$ represents the increase in the temperature of the film surface caused by the supplied heat (q_{exp}). The increase in temperature ($5 < \Delta T < 65 \text{ }^{\circ}\text{C}$) is recorded until it becomes constant at approximately 1200 s. The highest increase in temperature is observed for the pure Cu foil, regardless of the applied heating power, q_{exp} , (Fig. 6a–d). The natural-air convective cooling performances of the Cu foils with BiVO_4 micropillars are better than those of the pure Cu foils because the micropillars increase the overall surface area. The air-cooling properties are further enhanced with BiVO_4 micropillars electroplated with Ni; this can be observed on comparing the lines for Ni-0 and Ni-5 lines in Fig. 6. This cooling enhancement pattern appears for all q_{exp} values. An et al. [34] demonstrated that the cooling performances of oxidized Cu was superior to those of pure Cu nanofibers because of the increased surface area of the oxidized Cu decorated

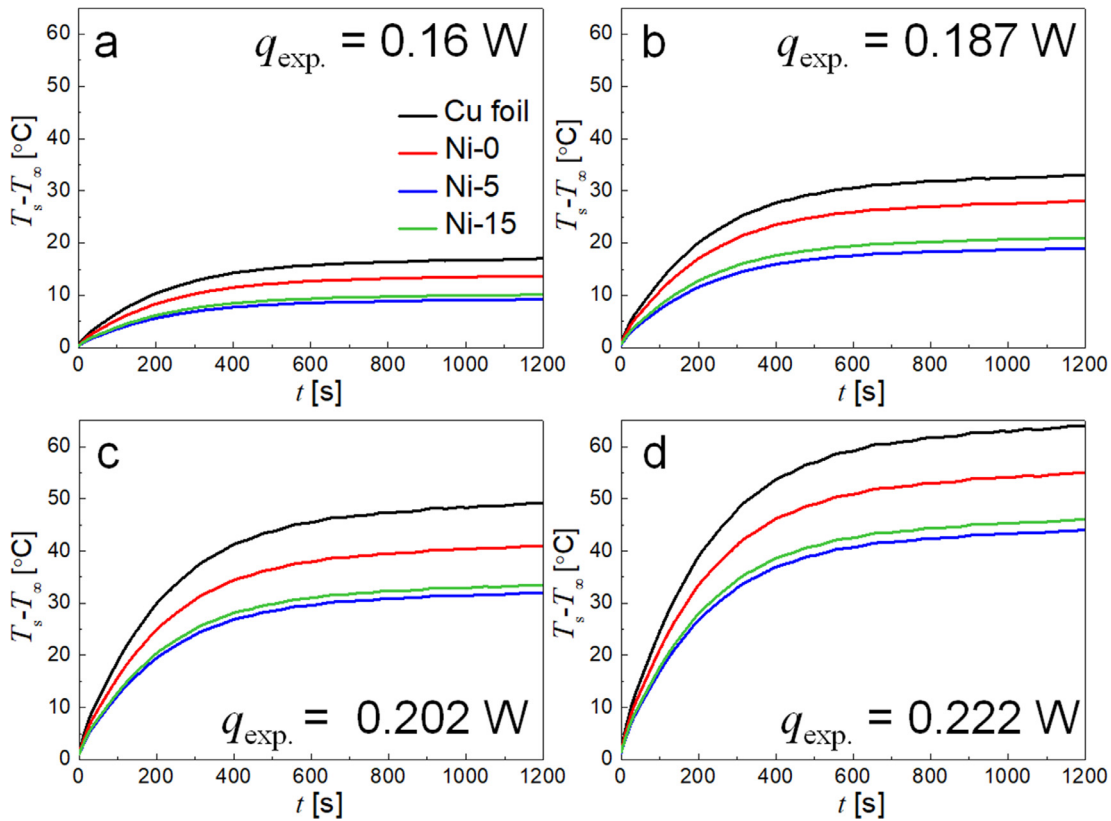


Fig. 6. Effect of electroplating time ($t_{ep} = 0, 5,$ and 15 min) on surface temperature (T_s) of Cu foil and BiVO_4 -Ni films (Ni-0, Ni-5, and Ni-15) at various heating powers (q_{exp}): (a) 0.160, (b) 0.187, (c) 0.202, and (d) 0.222 W. Here, T_∞ denotes the ambient temperature.

with thorny devil nanostructures. Similarly, in this study, a significant difference is observed between the cooling performance of Ni-0 and those of Ni-5 and Ni-15. When the BiVO_4 micropillars are electroplated, their mass is increased. Such an increase in mass causes morphological changes in the micropillars; these change the surface area and roughness of the cooling film, as shown in the SEM images in Fig. 7 (first column). Therefore, not only the material (metal vs. metal oxide) but also the increased surface area and roughness can contribute to the enhanced cooling performance of the BiVO_4 -Ni films.

Fig. 7a–c present the microstructures of the Ni-0, Ni-5, and Ni-15 films, wherein the top-, side-, and angle-views are presented in the first, second, and third columns, respectively. The BiVO_4 micropillars with highly textured surfaces promote efficient heat exchange between the film and the surrounding air. The numerous nanosized particles forming the micropillars can be observed in the top-view SEM image. These nanoparticles become less morphologically distinct as the electroplating time is increased.

The Ni-5 and Ni-15 films appear larger in height than the Ni-0 film; their height is increased from 5.79 to 6.63 μm . Therefore, their micropillars present larger surface areas. The similarity in ΔT of the Ni-5 and Ni-15 films in Fig. 6 may be attributed to the structural similarity of these two cases, as can be seen visually. This pattern in the film microstructures is consistent with the temperature measurements. Further increases in the electroplating time beyond 15 min is unnecessary because the empty spaces between the micropillars are narrowed as the electroplating time is increased. The micropillars thus form compact structures with significantly restricted air flow (Fig. 7). A further increase in the electroplating time would completely block the air flow; the film would eventually act as a thermal insulator with no air cooling performance. In addition, further increases in the micropillar

heights would increase the thermal resistance of the films because of the increased heat-transfer pathway lengths. Therefore, increasing the electroplating time beyond 15 min is unsubstantiated.

Fig. 8a depicts the electrical resistance R_e of the bare BiVO_4 film without nickel (i.e., Ni-0) as a function of the electroplating time. Here, the electroplating time increases from 15 to 30, 45, 60, and 75 min, which in turn increases the BiVO_4 film thickness and the micropillar height. The R_e is sharply increased with the electroplating time, as BiVO_4 is essentially a non-conductive material and therefore is a good electrical insulator. In Fig. 8a, R_e reaches approximately 3 Mega- Ω when the electroplating time exceeds 60 min. Note that none of these samples were electroplated with Ni; they were all Ni-0 films with different BiVO_4 thicknesses. In contrast, the electrical resistance of the Ni-5 and Ni-15 films is noted, in Fig. 8a, as $R_e = 6.7$ and 1.1 Ω , respectively, which is significantly lower than $R_e = 3.5$ Mega- Ω of the Ni-0 sample. In summary, the Ni-0 film was the non-conducting material while the Ni-5 and Ni-15 films were highly conducting films.

Fig. 8b presents the thermal resistance R_t of the Cu foil and Ni-0, Ni-5, and Ni-15 films at various q_{exp} levels. Here, R_t is estimated from $R_t = \Delta T/q_{exp}$, where $R_t = 1/(h_{eff} \cdot A_p)$; h_{eff} and A_p are the effective convective heat-transfer coefficient and projected surface area of the film, respectively. This expression is essentially the same as the Newton cooling law, $q_{exp} = h_{eff} \cdot A_p \cdot \Delta T$. Therefore, R_t represents the magnitude of the cooling capability of the films. If R_t is small, then h_{eff} is large and vice versa. In other words, small R_t values correspond to small ΔT and T_s values, which physically implies that T_s is decreased when cooling is more efficient. Conversely, the pure Cu foil yields the largest R_t values among all cases shown in Fig. 8b; this means the pure Cu foil case exhibited the least efficient cooling. With BiVO_4 and Ni, cooling efficiency increases with lowering R_t . The R_t values of the Ni-0 film

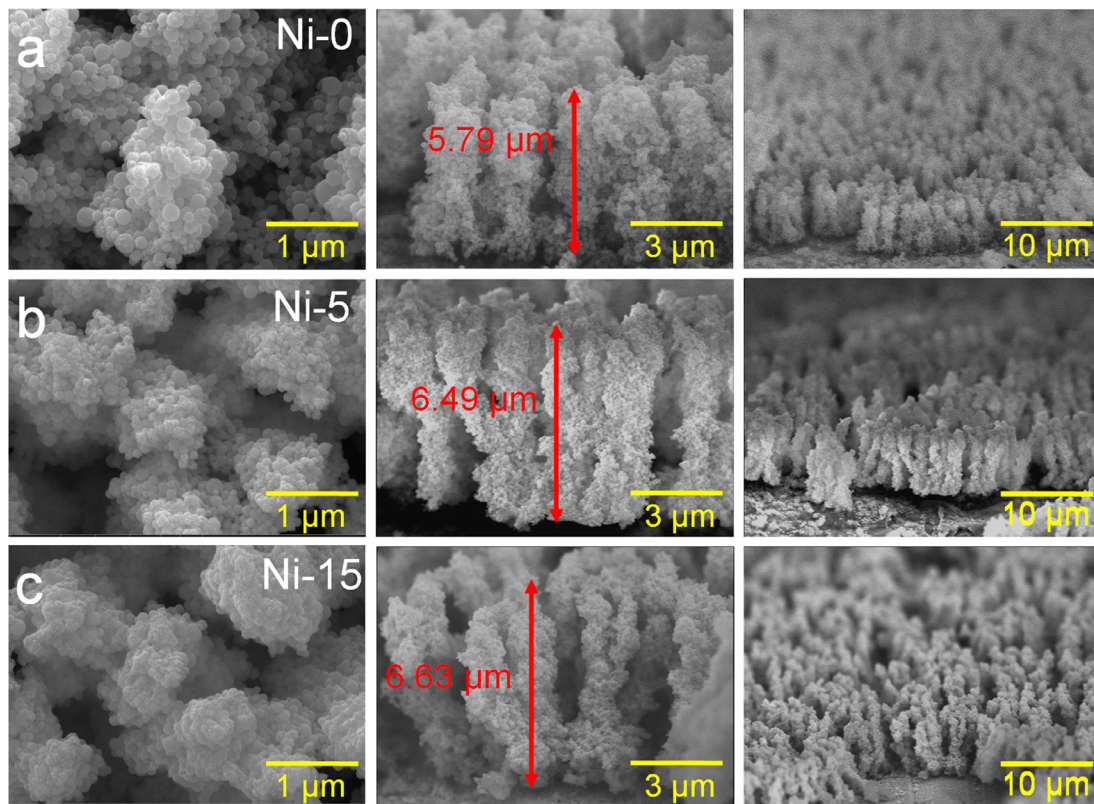


Fig. 7. SEM images of (a) bare BiVO_4 (Ni-0) and BiVO_4 electroplated with Ni for (b) 5 (Ni-5) and (c) 15 min (Ni-15).

are lower than those of the pure Cu foil (Fig. 8b). Furthermore, the R_t values of the Ni-5 and Ni-15 films are lower than those of the Ni-0 film because these cases present higher surface areas and roughness than the Ni-0 case, as previously mentioned (cf. Fig. 7). The differences in the R_t values between the Ni-5 and Ni-15 cases are small because their microstructures do not differ significantly (see Fig. 7). Hence, the effect of the nanoscale surface morphology of each pillar on the cooling performance appears to be negligible, whereas that of the microscale structure of the overall pillars appears more dominant on cooling (Figs 7 and 8b). It should be noted, in Fig. 8b, that R_t does not have to be constant at all q_{exp} values because ΔT and q_{exp} are nonlinear in relation. This nonlinearity arises because of the three-dimensional heat transfer phenomenon of the wire heating over a plate.

Fig. 8c and d present the IR images of the heated bare Cu foil and Ni-5 film ($3 \times 3 \text{ cm}^2$), respectively. A joule heating Cr wire is positioned under the sample at $q_{\text{exp}} = 0.2136 \text{ W}$ (cf. Fig. 2). At this heating level, the T_s of the pure Cu foil exceeds $90 \text{ }^\circ\text{C}$ after 400 s of heating. This temperature level is consistent with the quantitative observations reported in Fig. 6. At $t = 10 \text{ s}$, the centerline of the IR image of the bare Cu foil is brighter than that of the Ni-5 film. This is attributed to the greater thickness of the Ni-5 film because of the presence of the Ni-electroplated BiVO_4 micropillars. The thicker film initially prevents rapid heat transfer from the bottom of the film to the top surface. However, as heating continues, the heat is rapidly spread throughout the solid medium in both cases.

On the contrary, the overall T_s of the Ni-5 film is lower than that of the bare Cu foil (Fig. 8d) because the BiVO_4 micropillars increase the cooling efficiency of the film compared to that of the bare Cu foil. The difference in the peak temperature between the Cu foil and Ni-5 film is $\sim 20 \text{ }^\circ\text{C}$ or greater in some locations, which is a significant effect considering that a small temperature difference of only a few degrees can substantially improve the

performance of portable electronic devices by alleviating hotspot-induced malfunctions [34]. Because of its superior heat spreading capability, the temperature distribution of the Ni-5 film appears to be mild and uniform. Heat spreading is an important feature that could prevent the overheating-associated malfunction of electronic devices, particularly for completely sealed electronics with restricted air flow for natural convection. In such instances, the only alternative to heat removal is the efficient spreading of heat into the surroundings to alleviate thermal stress near the hotspots. Accordingly, this mild and uniform heat distribution under the same amount of heat is an additional advantage of the cooling film with the Ni-electroplated BiVO_4 micropillars.

Fig. 9a presents the changes in the electrical sheet resistance of the Ni-5 film with varied bending radii R_b of 1–16 mm. No significant changes in the electrical resistance of the film are observed even when R_b is decreased to 1 mm, demonstrating the excellent robustness of the mechanical properties of the film. In addition, Fig. 9b depicts the effects of the number of bending cycles on the electrical resistance of the Ni-5 film. Fig. S1 presents SEM images of the Ni-5 film after 500, 1000, 1500, and 2000 bending cycles; no sign of structural deterioration is observed. The electrical properties of the film are maintained even after 2000 bending cycles, indicating the outstanding mechanical reliability of the film and consequently its long lifespan.

Fig. 9c compares the spray cooling capabilities of the fabricated films. Atomized DI water droplets are sprayed onto the heated films at $T_s = 120 \text{ }^\circ\text{C}$ at $\Delta t = 30 \text{ s}$ intervals, and spraying is repeated 13 times until $t = 500 \text{ s}$. Because the surfaces of the films are hot, the droplets are evaporated upon contact, temporarily cooling the surfaces. Once evaporation is completed, T_s is increased again; this pattern repeats during the test. The spray cooling mechanism is attributed to the latent heat of vaporization of water; the water absorbs heat from the surface and thus cools it. The rise-and-fall pattern of T_s repeats, and the overall T_s is decreased for

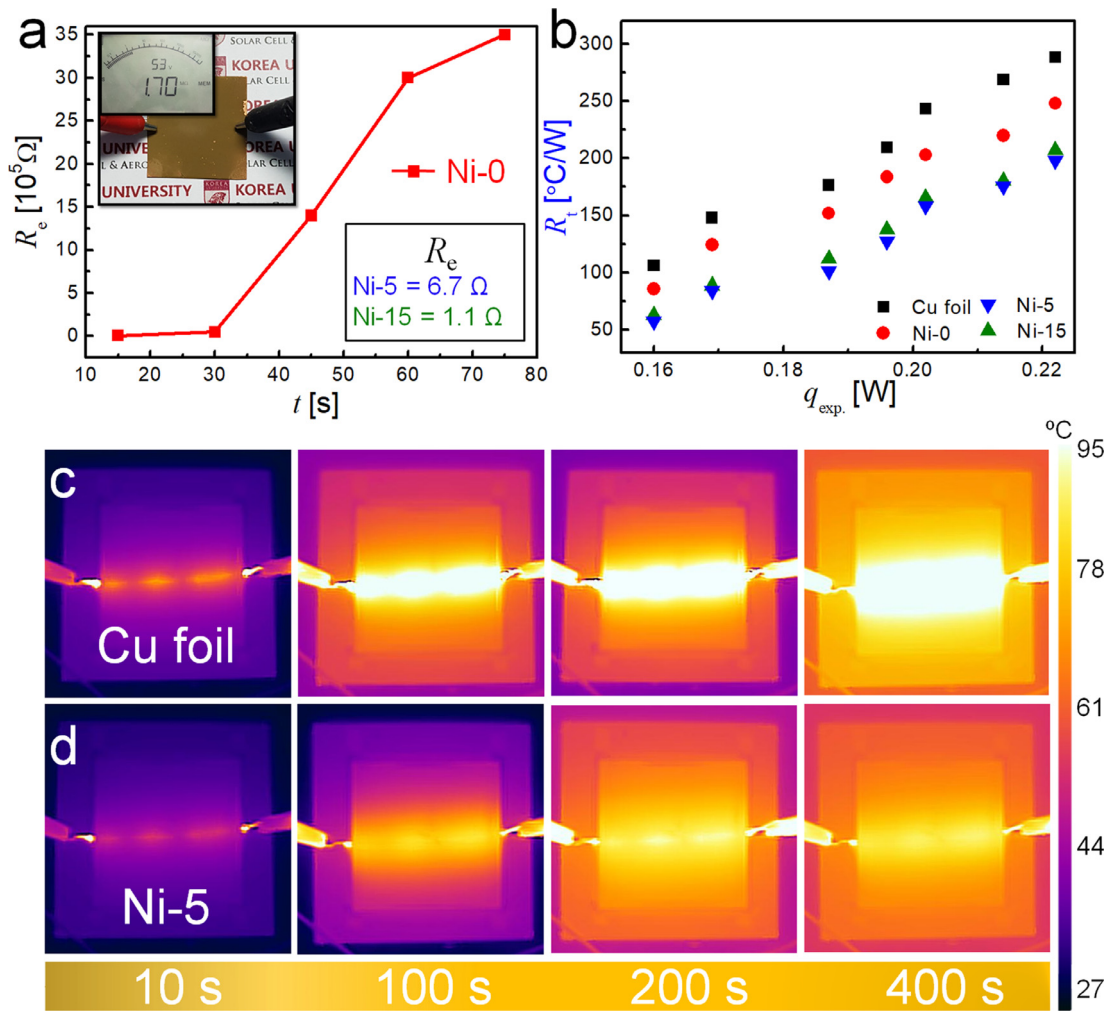


Fig. 8. (a) Electrospaying time-dependent electrical resistance (R_e) of the bare BiVO_4 film (i.e., Ni-0). (b) Thermal resistance (R_t) of Cu foil and Ni-0, Ni-5, and Ni-15 films at various heating power levels (q_{exp}); here, Ni-5 and Ni-15 denote BiVO_4 electroplated with Ni for 5 and 15 min, respectively. Infrared images of heated (c) pure Cu foil and (d) Ni-5 film at the heating power of $q_{\text{exp}} = 0.2136$ W. The size of the Cu foil is 3×3 cm^2 .

all films (Fig. 9c). The Ni-5 film exhibits the lowest T_s value (70 $^\circ\text{C}$) among all the films, 30 $^\circ\text{C}$ lower than that of the bare Cu foil (100 $^\circ\text{C}$) (see the inset image in Fig. 9c). Thus, it demonstrates that the temperature change can vary by up to ~ 30 $^\circ\text{C}$ depending on the surface texturing of the films. This significant difference in temperature is attributed to the different texturing conditions among the tested films. When the Cu foil is textured with BiVO_4 micropillars, its surface hydrophilicity is remarkably enhanced because of the roughening of the surface by the BiVO_4 micropillars, which facilitate the capture and holding of water (Wenzel model) [35]. In Fig. 9d, the water contact angles of the bare Cu foil, Ni-0, Ni-5, and Ni-15 films are compared; the Cu foil and Ni-5 film present the highest and lowest contact angles, respectively. Notably, the hydrophilicity of the film is even further enhanced with Ni electroplating of the BiVO_4 micropillars (see the Ni-5 case in Fig. 9d). However, for the Ni-15 case, the empty spaces between the micropillars in the Ni-15 film are too narrow to permit efficient water flow. As a result, the water contact angle is increased compared to that of the Ni-5 case. The effect of spray cooling for the Ni-15 film is also less prominent than that of the Ni-5 film (see Fig. 9c).

Fig. 9e illustrates the dynamic wetting conditions of the films, entailing a series of time-dependent photographs of a released single droplet impacting upon the heated surfaces ($T_s = 160$ $^\circ\text{C}$) of various films. The droplet has a diameter of $D_0 = 3$ mm and is released $H = 18$ cm above the film surface. The results obtained

at $T_s = 160$ $^\circ\text{C}$ are presented in Fig. 9e. The effect of T_s on the film wettability is negligible. The droplet collides with the film surface and splashes, forming fingers at the spreading rim of the droplet (see the images of the Cu foil in the first row). The diameter of the spreading liquid droplet for the bare Cu foil case is maximized at approximately 5 ms before recoiling; eventually, a droplet comparable in size with the initial droplet ($t = 0$ ms) forms. In contrast, for the Ni-5 film, the droplet spreading is maximized at $t \geq 9$ ms, confirming that the Ni-5 film is more hydrophilic than the Ni-0 film. In addition, no recoiling of the spreading droplet is observed for the Ni-5 film and the corresponding spreading area of the droplet is also large [36,37]. The larger spreading area and a thinner liquid film facilitate higher evaporation rate. This enhanced hydrophilicity facilitates the rapid evaporation of the sprayed droplets, as shown in Fig. 9c; thus, the rapid subsequent cooling of the film surfaces. The enhanced hydrophilicity of the electroplated films can be predicted by the Wenzel state, wherein the surface state enables the capturing and holding of liquid by imbibition, which is a common phenomenon on porous substrates [38–43]. In our case, the wettability change of the films is due to the change in the imbibition state, not the change in the substrate surface energy. This phenomenon is related with the “hydrodynamic focusing effect,” which prevents the receding motion of a spreading droplet through imbibition by microscopic pores.

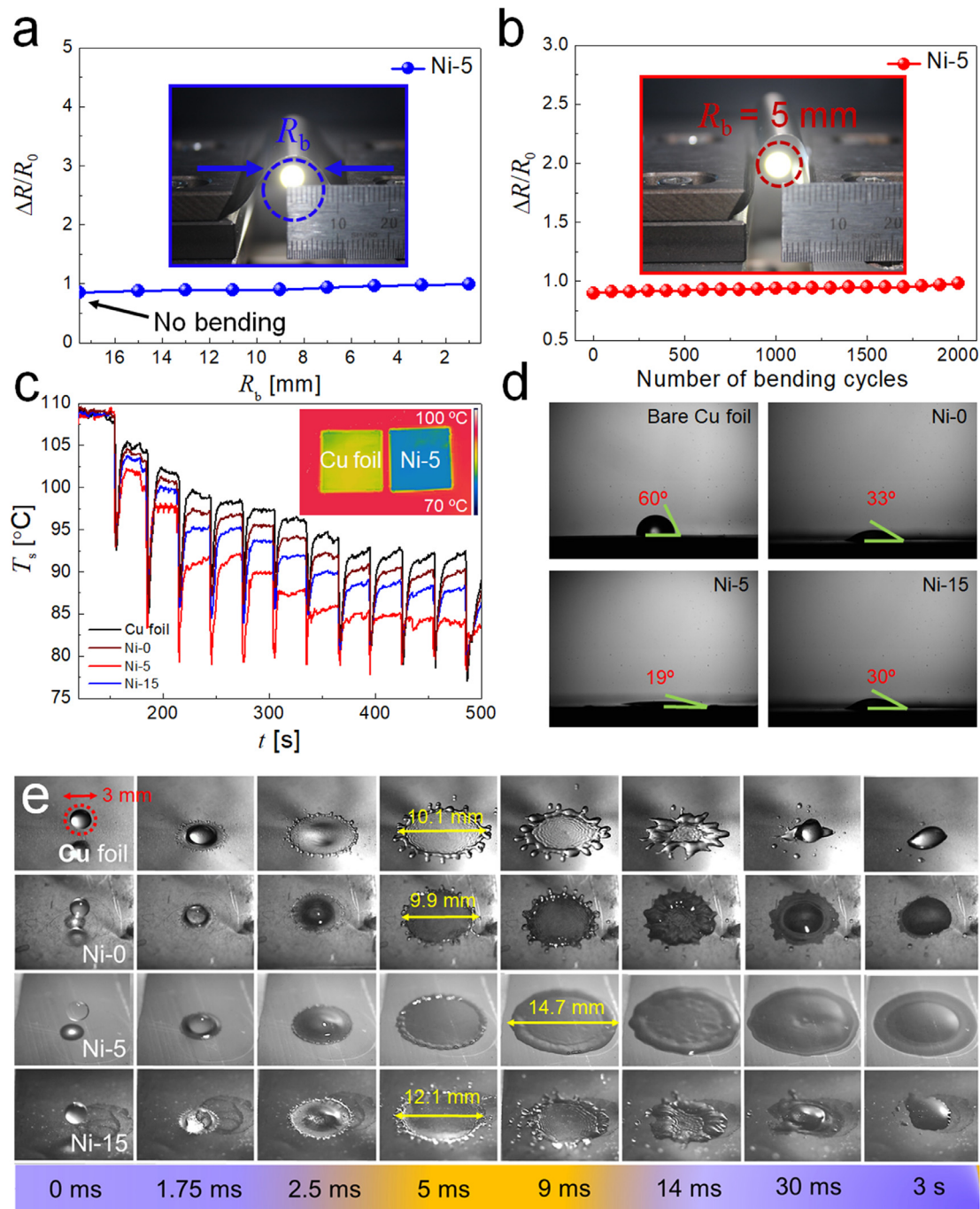


Fig. 9. (a) Changes in electrical sheet resistance ($\Delta R/R_0$) of Ni-5 film when the film is subjected to mechanical bending with the bending radius $R_b < 16$ mm. (b) Bending cycle (N) test with the fixed bending radius of $R_b = 5$ mm. (c) Decrease in surface temperature T_s of various films during spray cooling. The inset compares the bare (Cu foil) and Ni-5 films. (d) Water contact angles of various films. (e) Drop impact phenomena for various films at $T_s = 160$ °C.

Sahu et al. [44] reported a study of water droplet impact on suspended electrospun nanofiber membranes of various porosities and wetting behaviors. They showed that droplet impact was influenced by membrane thickness (varied from 8–10 μm) and pore size (varied from 3–6 μm). A droplet impact speed exceeding 3 m/s, involving dynamic impact over the time scale of a few milliseconds, caused membrane penetration regardless of the wettability of the mats. Therefore, the membrane wettability did not affect the droplet impact phenomena in high-speed impact scenarios when suspended membranes were used. However, for nanofiber mats attached to solid walls (non-suspended or unyielding substrates), the nanofiber mat wettability affected the droplet impact

behavior, even in high-speed dynamic impact scenarios. When entering the splashing regime at a high impact speed, the wettability effect was considerably clouded by the dominant splash phenomenon. In our current experiments, the substrate is unyielding (non-suspended), and the droplet impact speed is below the splashing regime; therefore, the substrate wettability significantly affects the droplet impact phenomena.

Table 2 compares the effective convective heat-transfer coefficients h_{eff} of air cooling for the bare Cu foil, Ni-0, Ni-5, and Ni-15 films at the heating power of $q_{\text{exp}} = 0.1958$ W. The value of h_{eff} changes as the surface roughness of the films is changed. When the surface is textured, the total surface area in contact with air

Table 2

Effective convective heat-transfer coefficients (h_{eff}) of various films at the heating power of $q_{\text{exp}} = 0.1958$ W. Here, R_t and A_p denote the thermal resistance and projected surface area of the film, respectively.

Material	h_{eff} [$\text{W m}^{-2} \text{K}^{-1}$]	Δh_{eff} w.r.t. $h_{\text{eff, Cu foil}}$ [%]	h_{eff}^{-1} or $R_t \cdot A_p$ [$\text{m}^2 \text{K W}^{-1}$]
Cu foil	5.95	-	0.17
Ni-0	6.79	13.6	0.15
Ni-5	9.78	64.4	0.10
Ni-15	9.05	52.1	0.11

is increased. However, an accurate estimation of the total surface area arising from the texturing cannot be achieved. To circumvent this, the projected surface area of the film A_p is assumed constant, while the effect of the increased surface area is incorporated into the effective heat transfer coefficient, h_{eff} . According to Newton's law of cooling, increased h_{eff} values imply that T_s is decreased:

$$h_{\text{eff}} = \frac{q}{A_p(T_s - T_\infty)}. \quad (1)$$

If both q and A_p are constant and h_{eff} is increased, then T_s must be decreased. Conversely, if T_s is increased due to poor cooling, then h_{eff} would decrease.

Note that the values of heat supplied is often relative because their absolute values are often offset by different measurement devices, which is acceptable for a relative comparison. However, when the accurate amount of heat supply is to be measured, the current (I) and voltage (V) must be independently measured; $q_{\text{exp}} = IV$. It is desirable that the measured q_{exp} value be confirmed by the empirically predicted q . The following empirical model serves well for estimating the power supplied to a heating wire:

$$q = h_b A_w (T_s - T_\infty), \quad (2)$$

where h_b is the heat-transfer coefficient of the air with respect to the cylindrical heating wire at $T_s = 69.1$ °C and $T_\infty = 28$ °C. The value of h_b is obtained considering the Nusselt number as $h_b = \text{Nu} \cdot k/d$. The surface area of the cylindrical heating wire A_w is calculated as $A_w = \pi \cdot d \cdot L$, where d and L are the diameter ($d = 1$ mm) and length of the wire ($L = 0.05$ m), respectively. The thermal conductivity of air is $k = 0.02945$ $\text{W m}^{-1} \text{K}^{-1}$, according to the temperature of the film T_f , which is defined as $T_f = (T_s + T_\infty)/2 = 48.55$ °C. In natural air convection, the value of Nu for a cylindrical heating wire can be estimated using an empirical formula that involves the Grashof (Gr) and Prandtl (Pr) numbers [45]:

$$\text{Gr} \cdot \text{Pr} = g\beta(T_s - T_\infty)d^3 \text{Pr} / \nu^2 \quad (3)$$

$$\text{Nu} = 1.02(\text{Gr} \cdot \text{Pr})^{0.148}, \quad (4)$$

where g is the gravitational acceleration (9.81 m s^{-2}) and β is the air thermal expansion coefficient, which is the reciprocal of T_f ; thus, $\beta = T_f^{-1} = 0.00311$ K^{-1} . Here, d is the characteristic length scale of a heat source; hence d is the heating wire diameter, $d = 1$ mm. Using the T_f value, Pr and the kinematic viscosity of air are estimated as $\nu = 0.7177$ and 0.00001995 $\text{m}^2 \text{s}^{-1}$, respectively [34]. Using the Nu value, determined using Eqs. (3) and (4), h_b is determined via the definition of Nu: $h_b = \text{Nu} \cdot k/L$. We substitute the h_b , A_w , and $(T_s - T_\infty)$ values in Eq. (2); thus, q is 0.22 W. Then, using $q = 0.22$ W, the h_{eff} values of all films (bare Cu, Ni-0, Ni-5, and Ni-15) are calculated as listed in Table 2. It should also be noted that the empirical $q = 0.22$ W and the measured $q_{\text{exp}} = 0.1958$ W differ by ~11%, confirming the accuracy of the empirical prediction.

The h_{eff} value of the bare Cu foil is $h_{\text{eff}} = 5.95$ $\text{W m}^{-2} \text{K}^{-1}$. The h_{eff} value of the Ni-0 film is approximately 14% higher than that of the bare Cu film. Furthermore, the h_{eff} value of the Ni-5 film is 64%

higher than that of the bare Cu foil. This is a significant improvement that enables us to control the surface temperature between 10 and 40 °C. This flexibility in temperature control leaves plenty of room for improvement of the hotspot-induced malfunctions for portable electronic devices.

4. Conclusion

Electrosprayed BiVO_4 micropillars were electroplated with Ni and characterized as flexible cooling films for potential use in microelectronic devices, which are subject to overheating and hotspot formation. An electroplating time of 5 min was determined to be optimal for producing an efficient cooling film with the lowest thermal resistance R_t and highest actual heat-transfer coefficient h_{actual} . The IR images of the fabricated bilayer films demonstrated that they could efficiently spread heat. A comparison of films with and without both BiVO_4 and Ni layers showed that the h_{actual} values of the Ni-0 and Ni-5 films were 14% and 64% higher, respectively, than that of the bare Cu foil. In addition, the BiVO_4 layer was electrically insulative; therefore, it can protect electronic devices from electrical shocks. These ceramic-metal bilayer films could facilitate both the electrical insulation and efficient air-cooling of electronic devices via their highly textured surfaces. When the fabricated films were subjected even to 2000 bending cycles, they exhibited little change in cooling performance and electrical insulation, thereby demonstrating their high mechanical robustness.

Acknowledgment

This research was supported by the Technology Development Program to Solve Climate Changes of the National Research Foundation (NRF) funded by the Ministry of Science, ICT & Future Planning (NRF-2016M1A2A2936760) and Advanced Research Center Program (NRF-2013R1A5A1073861). The research was also supported by the KU-FRG Program (K1822531).

Supplementary materials

Supplementary material associated with this article can be found, in the online version, at [doi:10.1016/j.ijheatmasstransfer.2020.119731](https://doi.org/10.1016/j.ijheatmasstransfer.2020.119731).

References

- [1] M. Iyengar, R. Schmidt, Analytical modeling for prediction of hot spot chip junction temperature for electronics cooling applications, in: Therm. Thermo-mech. Proc. 10th Intersoc. Conf. Phenom. Electron. Syst., 2006. IThERM., IEEE, 2006, pp. 87–95.
- [2] P. Wang, A. Bar-Cohen, On-chip hot spot cooling using silicon thermoelectric microcoolers, J. Appl. Phys. 102 (3) (2007) 034503.
- [3] A.L. Moore, L. Shi, Emerging challenges and materials for thermal management of electronics, Mater. Today 17 (4) (2014) 163–174.
- [4] L.-T. Yeh, R.C. Chu, Thermal management of microelectronic equipment: heat transfer theory, analysis methods, and design practices, ASME Press Book Series on Electronic Packaging, ASME International, New York, 2002, p. 414.
- [5] B. Yang, P. Wang, A. Bar-Cohen, Mini-contact enhanced thermoelectric cooling of hot spots in high power devices, IEEE Trans. Compon. Packag. Technol. 30 (3) (2007) 432–438.

- [6] E. Pop, S. Sinha, K.E. Goodson, Heat generation and transport in nanometer-scale transistors, *Proc. IEEE* 94 (8) (2006) 1587–1601.
- [7] R. Mahajan, C.-P. Chiu, G. Chrysler, Cooling a microprocessor chip, *Proc. IEEE* 94 (8) (2006) 1476–1486.
- [8] H.F. Hamann, A. Weger, J.A. Lacey, Z. Hu, P. Bose, E. Cohen, J. Wakil, Hotspot-limited microprocessors: direct temperature and power distribution measurements, *IEEE J. Solid-State Circuits* 42 (1) (2006) 56–65.
- [9] B. Hoefflinger, ITRS: the international technology roadmap for semiconductors, in: *Chips 2020*, Springer, 2011, pp. 161–174.
- [10] S.M. Sri-Jayantha, G. McVicker, K. Bernstein, J.U. Knickerbocker, Thermomechanical modeling of 3D electronic packages, *IBM J. Res. Dev.* 52 (6) (2008) 623–634.
- [11] B. Agostini, M. Fabbri, J.E. Park, L. Wojtan, J.R. Thome, B. Michel, State of the art of high heat flux cooling technologies, *Heat Transf. Eng.* 28 (4) (2007) 258–281.
- [12] R. Pfahl, J. McElroy, The 2004 international electronics manufacturing initiative (iNEMI) technology roadmaps, in: 2005 Conference on High Density Microsystem Design and Packaging and Component Failure Analysis, IEEE, 2005, pp. 1–7.
- [13] S. Sinha, P. Schelling, S. Phillpot, K. Goodson, Scattering of g-process longitudinal optical phonons at hotspots in silicon, *J. Appl. Phys.* 97 (2) (2005) 023702.
- [14] T. Cader, D. Tilton, Implementing spray cooling thermal management in high heat flux applications, in: The Ninth Intersociety Conference on Thermal and Thermomechanical Phenomena In Electronic Systems (IEEE Cat. No. 04CH37543), IEEE, 2004, pp. 699–701.
- [15] T. Harman, P. Taylor, M. Walsh, B. LaForge, Quantum dot superlattice thermoelectric materials and devices, *Science* 297 (5590) (2002) 2229–2232.
- [16] R. Venkatasubramanian, E. Siivola, T. Colpitts, B. O'quinn, Thin-film thermoelectric devices with high room-temperature figures of merit, *Nature* 413 (6856) (2001) 597.
- [17] X. Fan, G. Zeng, C. LaBounty, J.E. Bowers, E. Croke, C.C. Ahn, S. Huxtable, A. Majumdar, A. Shakouri, SiGeC/Si superlattice microcoolers, *Appl. Phys. Lett.* 78 (11) (2001) 1580–1582.
- [18] R.S. Prasher, J.-Y. Chang, I. Sauciu, S. Narasimhan, D. Chau, G. Chrysler, A. Myers, S. Prstic, C. Hu, Nano and micro technology-based next-generation package-level cooling solutions, *Intel Technol. J.* 9 (4) (2005) 285–286.
- [19] A. Bar-Cohen, P. Wang, On-chip hot spot remediation with miniaturized thermoelectric coolers, *Microgravity Sci. Technol.* 21 (1) (2009) 351–359.
- [20] H. Yoon, M.G. Mali, J.Y. Choi, M.-w. Kim, S.K. Choi, H. Park, S.S. Al-Deyab, M.T. Swihart, A.L. Yarin, S.S. Yoon, Nanotextured pillars of electrospayed bis-muth vanadate for efficient photoelectrochemical water splitting, *Langmuir* 31 (12) (2015) 3727–3737.
- [21] M.-W. Kim, K. Kim, T.Y. Ohm, H. Yoon, B. Joshi, E. Samuel, M.T. Swihart, S.K. Choi, H. Park, S.S. Yoon, Electrospayed BiVO₄ nanopillars coated with atomic-layer-deposited ZnO/TiO₂ as highly efficient photoanodes for solar water splitting, *Chem. Eng. J.* 333 (2018) 721–729.
- [22] M.G. Mali, H. Yoon, M.-W. Kim, M.T. Swihart, S.S. Al-Deyab, S.S. Yoon, Electrospayed heterojunction WO₃/BiVO₄ films with nanotextured pillar structure for enhanced photoelectrochemical water splitting, *Appl. Phys. Lett.* 106 (15) (2015) 151603.
- [23] S. Ghosh, I. Calizo, D. Teweldebrhan, E.P. Pokatilov, D.L. Nika, A.A. Balandin, W. Bao, F. Miao, C.N. Lau, Extremely high thermal conductivity of graphene: Prospects for thermal management applications in nanoelectronic circuits, *Appl. Phys. Lett.* 92 (15) (2008) 151911.
- [24] K.M. Shahil, A.A. Balandin, Thermal properties of graphene and multilayer graphene: applications in thermal interface materials, *Solid State Commun.* 152 (15) (2012) 1331–1340.
- [25] K.M. Shahil, A.A. Balandin, Graphene–multilayer graphene nanocomposites as highly efficient thermal interface materials, *Nano Lett.* 12 (2) (2012) 861–867.
- [26] Q.Q. Kong, Z. Liu, J.G. Gao, C.M. Chen, Q. Zhang, G. Zhou, Z.C. Tao, X.H. Zhang, M.Z. Wang, F. Li, Hierarchical graphene–carbon fiber composite paper as a flexible lateral heat spreader, *Adv. Funct. Mater.* 24 (27) (2014) 4222–4228.
- [27] N.-J. Song, C.-M. Chen, C. Lu, Z. Liu, Q.-Q. Kong, R. Cai, Thermally reduced graphene oxide films as flexible lateral heat spreaders, *J. Mater. Chem. A* 2 (39) (2014) 16563–16568.
- [28] M. Shtein, R. Nativ, M. Buzaglo, O. Regev, Graphene-based hybrid composites for efficient thermal management of electronic devices, *ACS Appl. Mater. Interfaces* 7 (42) (2015) 23725–23730.
- [29] Y. Zhang, H. Han, N. Wang, P. Zhang, Y. Fu, M. Murugesan, M. Edwards, K. Jeppson, S. Volz, J. Liu, Improved heat spreading performance of functionalized graphene in microelectronic device application, *Adv. Funct. Mater.* 25 (28) (2015) 4430–4435.
- [30] S. Sinha-Ray, Y. Zhang, A.L. Yarin, Thorny devil nanotextured fibers: the way to cooling rates on the order of 1 kW/cm², *Langmuir* 27 (1) (2010) 215–226.
- [31] C.M. Weickgenannt, Y. Zhang, S. Sinha-Ray, I.V. Roisman, T. Gambaryan-Roisman, C. Tropea, A.L. Yarin, Inverse-Leidenfrost phenomenon on nanofiber mats on hot surfaces, *Phys. Rev. E* 84 (3) (2011) 036310.
- [32] T.-G. Kim, C.-W. Park, D.-Y. Woo, S.S. Yoon, Efficient heat spreader using superpersonally sprayed graphene and silver nanowire, *Appl. Therm. Eng.* (2019) 114572.
- [33] S. Husain, F. Rahman, N. Ali, P. Alvi, Nickel sub-lattice effects on the optical properties of ZnO nanocrystals, *J. Optoelectron. Eng.* 1 (1) (2013) 28–32.
- [34] S. An, H.S. Jo, S.S. Al-Deyab, A.L. Yarin, S.S. Yoon, Nano-textured copper oxide nanofibers for efficient air cooling, *J. Appl. Phys.* 119 (6) (2016) 065306.
- [35] S. An, B.N. Joshi, J.-G. Lee, M.W. Lee, Y.I. Kim, M.-W. Kim, H.S. Jo, S.S. Yoon, A comprehensive review on wettability, desalination, and purification using graphene-based materials at water interfaces, *Catal. Today* 295 (2017) 14–25.
- [36] A.S. Kousalya, K.P. Singh, T.S. Fisher, Heterogeneous wetting surfaces with graphitic petal-decorated carbon nanotubes for enhanced flow boiling, *Int. J. Heat Mass Transf.* 87 (2015) 380–389.
- [37] H.S. Jo, J.-G. Lee, S. An, T.G. Kim, S.C. James, J. Choi, S.S. Yoon, Supersonically sprayed, triangular copper lines for pool boiling enhancement, *Int. J. Heat Mass Transf.* 113 (2017) 210–216.
- [38] A.N. Lembach, H.-B. Tan, I.V. Roisman, T. Gambaryan-Roisman, Y. Zhang, C. Tropea, A.L. Yarin, Drop impact, spreading, splashing, and penetration into electrospun nanofiber mats, *Langmuir* 26 (12) (2010) 9516–9523.
- [39] C.M. Weickgenannt, Y. Zhang, A.N. Lembach, I.V. Roisman, T. Gambaryan-Roisman, A.L. Yarin, C. Tropea, Nonisothermal drop impact and evaporation on polymer nanofiber mats, *Phys. Rev. E* 83 (3) (2011) 036305.
- [40] S. Sinha-Ray, S. Sinha-Ray, A.L. Yarin, C.M. Weickgenannt, J. Emmert, C. Tropea, Drop impact cooling enhancement on nano-textured surfaces. Part II: Results of the parabolic flight experiments [zero gravity (0g) and supergravity (1.8 g)], *Int. J. Heat Mass Transf.* 70 (2014) 1107–1114.
- [41] S. Sinha-Ray, A.L. Yarin, Drop impact cooling enhancement on nano-textured surfaces. Part I: theory and results of the ground (1g) experiments, *Int. J. Heat Mass Transf.* 70 (2014) 1095–1106.
- [42] A.L. Yarin, I.V. Roisman, C. Tropea, *Collision Phenomena in Liquids and Solids*, Cambridge University Press, 2017.
- [43] R. Sahu, S. Sett, A.L. Yarin, B. Pourdeyhimi, Impact of aqueous suspension drops onto non-wettable porous membranes: hydrodynamic focusing and penetration of nanoparticles, *Colloids Surf., A* 467 (2015) 31–45.
- [44] R.P. Sahu, S. Sinha-Ray, A.L. Yarin, B. Pourdeyhimi, Drop impacts on electrospun nanofiber membranes, *Soft Matter* 8 (14) (2012) 3957–3970.
- [45] J.P. Holman, J.P. Holman, *Heat Transfer*, McGraw-Hill Companies, 1976.